iScience

CellPress
OPEN ACCESS

Article

Topological superconductivity and large spin Hall effect in the kagome family Ti_6X_4 (X = Bi, Sb, Pb, Tl, and In)

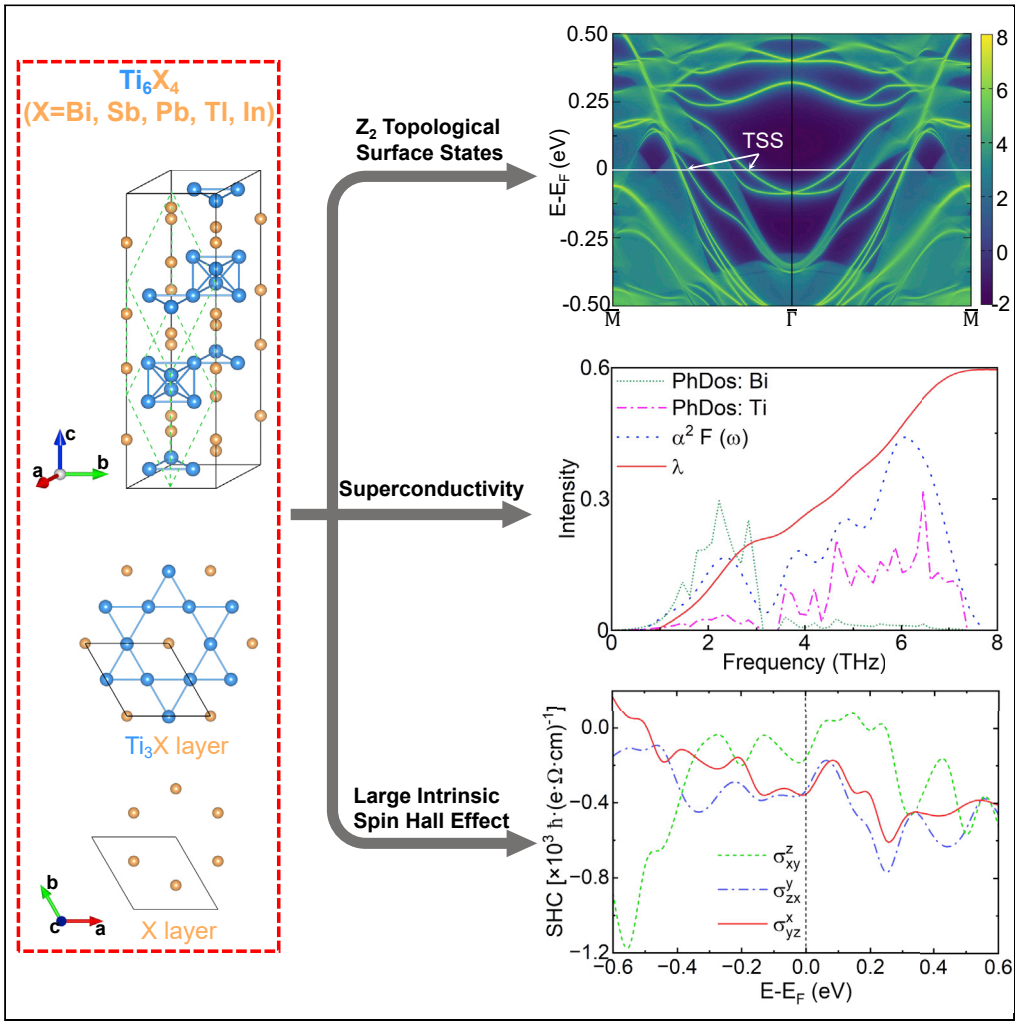

Xin-Wei Yi, Zheng-Wei Liao, Jing-Yang You, Bo Gu, Gang Su

phyjyy@nus.edu.sg (J.-Y.Y.)
gubo@ucas.ac.cn (B.G.)
gsu@ucas.ac.cn (G.S.)

Highlights

Five stable nonmagnetic kagome compounds Ti_6X_4 (X = Bi, Sb, Pb, Tl, and In) are predicted

Ti_6X_4 exhibit superconductivity with critical temperature Tc = 3.8 K–5.1 K

Ti_6X_4 have nontrivial Z_2 band topology, and topological surface states near E_F

Ti_6X_4 display large intrinsic spin Hall conductivity of 34–639 $\hbar \cdot (e \cdot \Omega \cdot cm) - 1$

Yi et al., iScience 26, 105813
January 20, 2023
https://doi.org/10.1016/j.isci.2022.105813

iScience

CellPress
OPEN ACCESS

Article

Topological superconductivity and large spin Hall effect in the kagome family Ti_6X_4 (X = Bi, Sb, Pb, Tl, and In)

Xin-Wei Yi,[1] Zheng-Wei Liao,[1] Jing-Yang You,[2,*] Bo Gu,[1,3,*] and Gang Su[1,3,4,*]

SUMMARY

Topological superconductors (TSC) become a focus of research due to the accompanying Majorana fermions. However, the reported TSC are extremely rare. Recent experiments reported kagome TSC AV_3Sb_5 (A = K, Rb, and Cs) exhibit unique superconductivity, topological surface states (TSS), and Majorana bound states. More recently, the first titanium-based kagome superconductor $CsTi_3Bi_5$ with nontrivial topology was successfully synthesized as a perspective TSC. Given that Cs contributes little to electronic structures of $CsTi_3Bi_5$ and binary compounds may be easier to be synthesized, here, by first-principle calculations, we predict five stable nonmagnetic kagome compounds Ti_6X_4 (X = Bi, Sb, Pb, Tl, and In) which exhibit superconductivity with critical temperature Tc = 3.8 K − 5.1 K, nontrivial $\mathbb{Z}_2$ band topology, and TSS close to the Fermi level. Additionally, large intrinsic spin Hall effect is obtained in Ti_6X_4, which is caused by gapped Dirac nodal lines due to a strong spin-orbit coupling. This work offers new platforms for TSC and spintronic devices.

INTRODUCTION

Topological superconductor (TSC) with Majorana fermions becomes an important subject in condensed matter physics.[1] Their topological gapless excitations of linear dispersion and particle-hole symmetry can naturally meet the two requirements of Majorana fermion, where excitations obey the Dirac equation and particles are equal to their own anti-particles.[2] The Majorana fermion in TSC following non-Abelian statistics is promising for topological quantum computations without decoherence.[3,4] Two possible approaches to achieve TSC are odd-parity superconductors with inherently strong topology[5,6] and superconducting proximity effect.[7–9] Experimental detection of surface Andreev bound states and theoretical analysis have given supporting information of the topological superconductivity in the odd-parity superconductors $Cu_xBi_2Se_3$[10–12] and $Sn_{1-x}In_xTe$.[13] The proximity effect has focused on proximity-induced coupling of s-wave superconductors with topological insulators[7] or semiconductors with strong spin-orbit coupling (SOC).[8,9] Several artificially fabricated heterostructures and nanowires have revealed evidences of the Majorana fermions along this route, including epitaxial Bi_2Te_3 films grown on $NbSe_2$,[14–16] InAs nanowires segment with epitaxial Al,[17] InSb nanowires contacted with NbTiN,[18] and Fe atomic chains on the surface of Pb.[19] Additionally, some materials with both bulk superconductivity and surface topological Dirac cones can also intrinsically establish this proximity effect.[20–25] Majorana zero modes has been observed in this kind of intrinsic TSC, including the iron-based superconductors − FeTe 1 − x Se_x,[26–30] $CaKFe_4As_4$,[31] LiFeAs,[32,33] and van der Waals material 2M-WS_2.[34] In terms of fabrication, the intrinsic TSC is more promising than the heterostructures and nanowires. Additionally, both experimental and predicted intrinsic TSC are extremely rare and most of them can only achieve superconductivity or suitable topological surface states (TSS) near the Fermi energy (E_F) by doping. Finding more intrinsic TSC candidates with high Tc and TSS in the vicinity of E_F is highly urgent.

Recently, robust Majorana bound states were observed in a new kagome superconductor CsV_3Sb_5[35] as a new paradigm of intrinsic TSC. This new superconductor family AV_3Sb_5 (A = K, Rb, and Cs) exhibit unique superconductivity with superconducting transition temperatures (Tc) of 0.9 − 2.5 K at ambient pressure,[36–48] a nontrivial $\mathbb{Z}_2$ topology,[36,49] and other new quantum properties.[50–55] Very recently, the first Ti-based kagome $CsTi_3Bi_5$ with the AV_3Sb_5 prototype structure has also been synthesized experimentally[56] following theoretical prediction,[57] and it exhibits a Tc of about 4.8 K, which is much higher than that of

[1]School of Physical Sciences, University of Chinese Academy of Sciences, Beijing 100049, China

[2]Department of Physics, Faculty of Science, National University of Singapore, Singapore 117551, Singapore

[3]Kavli Institute for Theoretical Sciences, CAS Center for Excellence in Topological Quantum Computation, University of Chinese Academy of Sciences, Beijing 100190, China

[4]Lead contact

*Correspondence: phyjyy@nus.edu.sg (J.-Y.Y.), gubo@ucas.ac.cn (B.G.), gsu@ucas.ac.cn (G.S.)

https://doi.org/10.1016/j.isci.2022.105813

AV_3Sb_5.[56] It was predicted that $CsTi_3Bi_5$ has nontrivial band topology and robust TSS, implying a possible TSC similar to AV_3Sb_5. It is very intriguing to find more candidates of TSC with high Tc and intrinsic TSS in similar Ti-based kagome systems. Considering that the density of states (DOS) in $CsTi_3Bi_5$ near E_F is mainly contributed by Ti atoms while Cs has almost no contribution and in general binary compounds are also easier to be synthesized in experiments, it will be interesting and imperative to study the Ti-based binary compounds.

In this paper, by density functional theory (DFT) calculations, we predicted kagome nonmagnetic family Ti_6X_4 (X = Bi, Sb, Pb, Tl, and In). Ti_6X_4 are stacked by Ti-based kagome layers and X-based honeycomb layers similar to $CsTi_3Bi_5$. The low E_{hull} in energy convex hull and phonon spectra without imaginary frequency of Ti_6X_4 show the evidences of their thermodynamic and dynamic stability. The nontrivial $\mathbb{Z}_2$ index and corresponding TSS near E_F with spin-moment-locked spin textures demonstrate that they are ideal $\mathbb{Z}_2$ topological metals. On the other hand, the calculated electron-phonon coupling (EPC) based on the Bardeen-Cooper-Schrieffer (BCS) theory suggests that they have superconducting transitions with a transition temperature Tc of 3.9 – 5.1 K. The coexistence of superconductivity with high Tc and ideal TSS offers promising platforms for realizing TSC and Majorana fermions. Moreover, the band structures of Ti_6X_4 show abundant Dirac nodes and Dirac nodal lines (DNLs), all of which have gaps in the presence of the strong SOC. The calculated intrinsic spin Hall conductivity (SHC) shows that these gapped nodes and DNLs contribute to a large SHC in Ti_6X_4, where SHC of Ti_6Bi_4 and Ti_6Sb_4 can reach 354 and 629 $\hbar \cdot (e \cdot \Omega \cdot cm)^{-1}$, respectively.

RESULTS FOR Ti_6Bi_4

Crystal structure of Ti_6Bi_4

$CsTi_3Bi_5$ is a layered material,[56] consisting of Bi and Ti_3Bi layers, as shown in Figure 1B. The structure of Ti_6Bi_4 can be obtained by stacking these atomic layers as seen in Figure 1A, where different Ti_3Bi layers stacked in the "c" direction have in-plane sliding and the two Ti_3Bi layers are sandwiched by Bi honeycomb layers. It should be noticed that the Ti kagome nets have some breathing distortions, where the triangles of kagome nets are divided into two unequal sizes. Ti_6Bi_4 has a rhombohedral structure with a space group of R $\bar{3}$ m (No.166). Its Bravais and primitive lattices are represented by black solid and green dotted lines in Figure 1A, respectively. The bulk Brillouin zone (BZ) and high symmetry points are plotted in Figure 1D, where four inequivalent time-reversal invariant momenta (TRIM) points are labeled as Γ, T, F, and L.

By calculating the formation energies E_f of all Ti-Bi binary systems,[58–60] we can draw the convex hull as shown in Figure 1C. We can see that Ti_6Bi_4 is thermodynamically stable with E_{hull} = 0 meV. Among all these binary Ti-Bi compounds listed in Figure 1C, only Ti_6Bi_4 has kagome nets. Its special structure similar to CsV_3Sb_5 and $CsTi_3Bi_5$ makes Ti_6Bi_4 become promising materials to explore the possible intrinsic topological superconductors. The experimental synthesis of a new phase of Ti_3Bi_2 was reported, where the elements ratio of Ti:Bi = 3:2 was obtained by the energy dispersive X-ray spectroscopy but its exact structure has not been determined.[61] It indicates that our predicted Ti_6Bi_4 may already be fabricated in the experiment.

Electronic band structure and topological properties

The electronic band structure of Ti_6Bi_4 without SOC is plotted in Figure S1. Many degenerated points can be seen and some of them are not isolated but form DNLs as seen in Figure S3. The electronic energy bands and partial DOS with SOC for Ti_6Bi_4 are plotted in Figure 1A. Comparing the electronic band structure without SOC in Figure S1, SOC lifts the degeneracy at the Dirac nodes and DNLs, which generates a continuous bandgap between two adjacent energy bands in the whole BZ. The DOS exhibits an obvious valley near the Fermi energy and the projected DOS of Ti atoms is much larger than that of Bi atoms. The band structure with weights of projected different orbitals of Ti and Bi atoms is shown in Figure S2 in supplemental information. The bands near the Fermi level are dominated by the 5d orbitals of Ti and the 3p orbitals of Bi, while the s orbitals of Ti and Bi have little contributions. Experimental angle-resolved photoemission spectroscopy (ARPES) measurement and the DFT calculations of the V-based kagome structures quantitatively give similar electronic band structures, indicating the validity of the calculated band structures by DFT in these types of systems.[36]

With the time-reversal and inversion symmetries of Ti_6Bi_4, its strong $\mathbb{Z}_2$ topological invariant can be calculated by the parity of wavefunctions at all TRIM points.[62] Moreover, other three weak $\mathbb{Z}_2$ topological invariants can also be calculated. It can be seen from Figure 2B that several energy bands, including bands 73, 75, and 79 below the Fermi energy (E_F) have a strong $\mathbb{Z}_2$ index, resulting in abundant clear Dirac cone TSS near

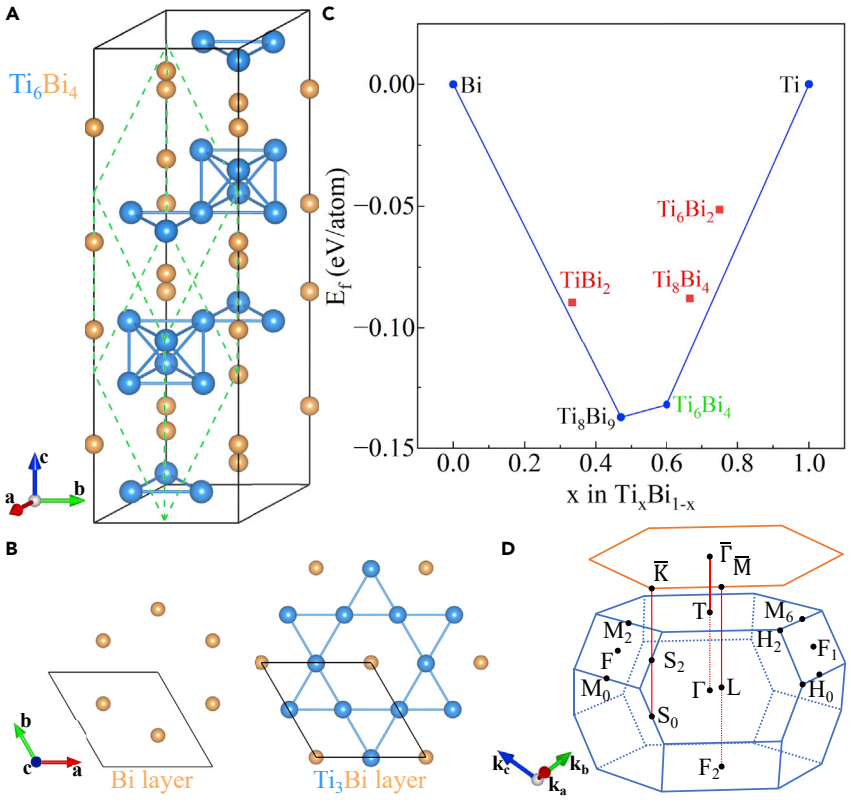

Figure 1. The crystal structure for Ti_6Bi_4 and the convex hull of Ti_xBi_{1-x}

(A) The crystal structure for Ti_6Bi_4 stacked by Ti_3Bi and Bi layers. The black solid and green dotted lines represent the Bravais and primitive lattices, respectively.

(B) Top view of Bi and Ti_3Bi atomic layers.

(C) The convex hull of Ti_xBi_{1-x}.

(D) Brillouin zone (BZ) with high symmetry points. 3D and 2D BZ are drawn with blue and orange solid lines, respectively.

the Fermi level in the surface spectrum functions as shown in Figure 2E. The nontrivial TSS and nontrivial $\mathbb{Z}_2$ index make Ti_6Bi_4 a $\mathbb{Z}_2$ topological metal.

Unlike most VSb-based kagome structures where the TSS are usually submerged in their bulk states, the bulk states of Ti_6Bi_4 have a large bandgap at "Γ" point near E_F, which makes its TSS clearly exist without entanglement with bulk states as shown in Figure 2A. The 3D Fermi surface (FS) is plotted in Figures 2C and 2D, where the electron pockets are concentrated near F, F_1, F_2, Γ, and T points. The electron pocket centered on the Γ point shows an obvious cylindrical surface along the direction perpendicular to the kagome net, which enables ARPES to easily measure the TSS near $\overline{\Gamma}$. With calculated surface Green's function for a semi-infinite system and the surface spectrum function, the spin texture of surface states at fixed energy can be directly obtained. The detailed methods can be seen in supplemental information. Therefore, we further draw the projected surface spectral functions and spin textures on (001) plane at E_F in Figure 2F. The TSS form multiple circles centered on the $\overline{\Gamma}$ point, which presents obvious spin-momentum locking, showing the existence of robust TSS near E_F again.

Superconductivity

Similar to CsV_3Sb_5 and $CsTi_3Bi_5$, the emergence of superconducting ground states in Ti_6Bi_4 is very promising. To study the superconductivity in Ti_6Bi_4, we first calculate its magnetic properties. We consider several typical collinear and noncollinear magnetic configurations, including one nonmagnetic configuration, three ferromagnetic, and three antiferromagnetic configurations along x, y, and z directions, respectively, and three classical antiferromagnetic configurations of bilayer kagome net as shown in Figure S4. By comparing the total energies and final magnetic moment per atom of these magnetic configurations, Ti_6Bi_4

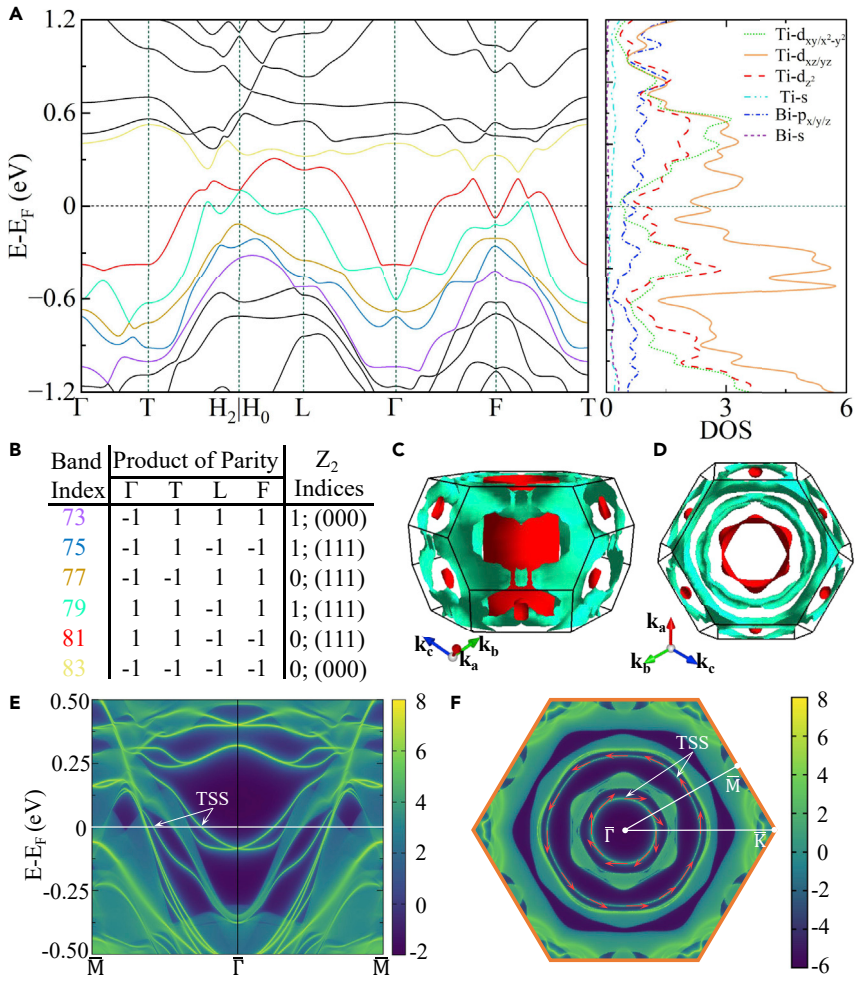

Band Index	Product of Parity Γ	T	L	F	Z_2 Indices
73	-1	1	1	1	1; (000)
75	-1	1	-1	-1	1; (111)
77	-1	-1	1	1	0; (111)
79	1	1	-1	1	1; (111)
81	1	1	-1	-1	0; (111)
83	-1	-1	-1	-1	0; (000)

Figure 2. The electronic band structure and topological surface states of Ti_6Bi_4

(A) The electronic band structure and partial density of states (DOS) with spin-orbit coupling (SOC) for Ti_6Bi_4. Different bands near the E_F are drawn in different colors.

(B) Product of parity for four inequivalent TRIM points and $\mathbb{Z}_2$ index of bands near Fermi level.

(C and D) Three-dimensional Fermi surface of Ti_6Bi_4 in (C) side and (D) top views.

(E) The surface spectrum functions along $\bar{M}$-$\bar{\Gamma}$-$\bar{M}$ paths projected on (001) plane for Ti_6Bi_4.

(F) Spin texture of topological surface states (TSS) projected on (001) plane for Ti_6Bi_4 at $E\text{-}E_F = 0$ meV.

can be identified as a nonmagnet. Furthermore, we calculate the Eliashberg spectral function $\alpha^2 F(\omega)$ and EPC $\lambda(\omega)$ (see Figure 3), then the EPC $\lambda(\omega = \infty)$ and Tc of Ti_6Bi_4 are estimated to be 0.586 and 3.8 K as listed in Table 1, respectively, which are relatively high values among the recently discovered kagome superconductors. From Figure 3, we find that the phonon DOS (PhDOS) at high frequency (~ 6 THz) and low frequency (~ 2 THz) is dominated by the contribution of Ti and Bi atoms, respectively. As a rough estimation, the contribution of Ti atoms vibration accounts for more than half of the total EPC. Since the mass of Ti atom is smaller than that of V atom, this partially explains the enhanced EPC and Tc in Ti-based kagome superconductors.

Spin Hall effect

The symmetry protected DNL in the energy band can serve as a source of various quantum phenomena, such as the spin Hall effect (SHE). The large SOC mixing different spin components of wave functions produces a big numerator, and the small gap of DNL induced by SOC contributes a small denominator in Equation 4 in supplemental information, so a large SHC may appear. Due to the large SOC and corresponding gapped DNLs, a large SHC in Ti_6Bi_4 is expected. The crystal symmetry of Ti_6Bi_4 constraints three

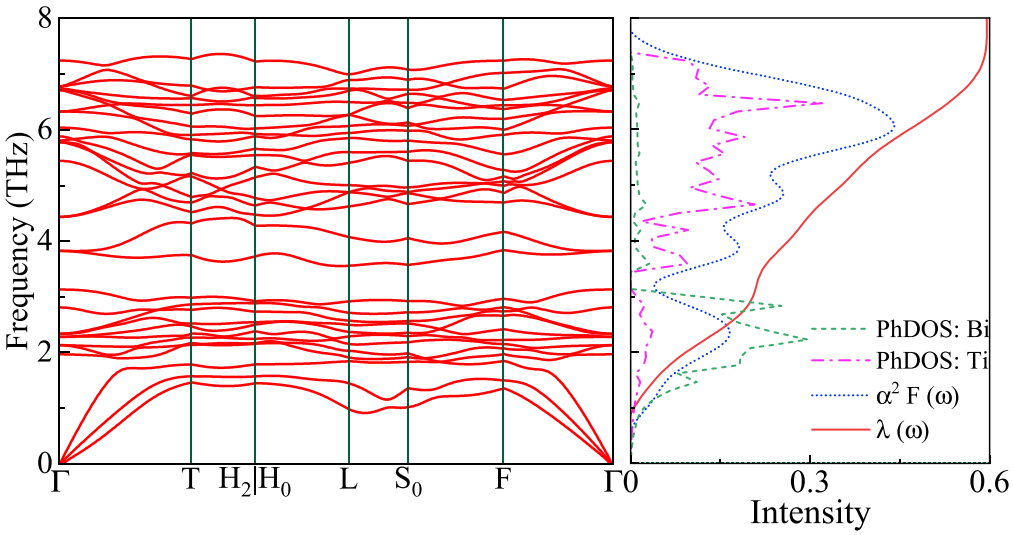

Figure 3. The superconductivity of Ti_6Bi_4

The phonon spectrum, projected phonon DOS (PhDOS), Eliashberg spectral function $\alpha^2 F(\omega)$, and cumulative frequency-dependent EPC $\lambda(\omega)$ for Ti_6Bi_4.

independent components of SHC tensor, i.e. $\sigma^z_{xy} = -\sigma^z_{yx}$; $\sigma^y_{zx} = -\sigma^x_{zy}$; $\sigma^x_{yz} = -\sigma^y_{xz}$.[63] Therefore, we evaluate three independent components σ^z_{xy}, σ^y_{zx}, and σ^x_{yz} as a function of chemical potential as plotted in Figure 4A. It can be seen that the magnitudes of three components are around $160 - 354\ \hbar\cdot(e\cdot\Omega\cdot cm)^{-1}$ at E_F. The SHC changes drastically with the change of chemical potential, and σ^z_{xy} can reach $1168\ \hbar\cdot(e\cdot\Omega\cdot cm)^{-1}$ at −0.55 eV.

To reveal the origin of large SHC, we plot the band structure of Ti_6Bi_4 colored by the magnitude of spin Berry curvature $\Omega^x_{n,yz}(\mathbf{k})$, as well as the k-resolved $\Omega^x_{yz}(\mathbf{k})$ at E_F in Figures 4B and 4C. It is noted that $\Omega^x_{n,yz}(\mathbf{k})$ strongly depends on wave vector $\mathbf{k}$, and $\Omega^x_{n,yz}(\mathbf{k})$ shows prominent peaks at positions of gapped nodes and DNLs, which mainly contribute to SHC. The reason for relatively isotropic SHC is that Dirac nodes and DNLs are located at different energy levels. The large SHC of Ti_6Bi_4 provides promising applications for spintronics.

RESULTS FOR KAGOME FAMILY Ti_6X_4 (X = SB, PB, TL, AND IN)

To our knowledge, $CsTi_3Bi_5$ exhibits many interesting properties and is the only superconductor with titanium-based kagome net.[56] Therefore, it is important to find more titanium-based kagome superconductors. In the Ti_6Bi_4, the electronic states near the E_F are mainly contributed by Ti atoms, which indicate that the substitution of Bi atoms may produce the family Ti_6X_4, similar to Ti_6Bi_4. We substitute Bi in Ti_6Bi_4 with all elements of groups IIIA, IVA, VA, and VIA except radioactive polonium, and find four dynamically stable compounds Ti_6X_4 (X = Sb, Pb, Tl, and In). Furthermore, DFT calculations show that Ti_6Sb_4, Ti_6Pb_4, and Ti_6Tl_4 are all thermodynamically stable with E_{hull} = 0 eV, and Ti_6In_4 also has a relatively small E_{hull} =

Table 1. Electronic DOS at the Fermi energy $N(E_F)$ (states/(eV · f.u.)), electron-phonon coupling EPC λ ($\omega = \infty$), logarithmically averaged phonon frequency ω_{log}, and estimated Tc for Ti_6X_4

Structures	$N(E_F)$ (states/(eV · f.u.))	λ	ω_{log} (K)	T_c (K)
Ti_6Bi_4	5.707	0.586	177.3	3.8
Ti_6Sb_4	5.153	0.617	187.8	4.7
Ti_6Pb_4	5.836	0.642	172.0	4.8
Ti_6In_4	5.854	0.604	166.8	3.9
Ti_6Tl_4	6.225	0.666	166.0	5.1

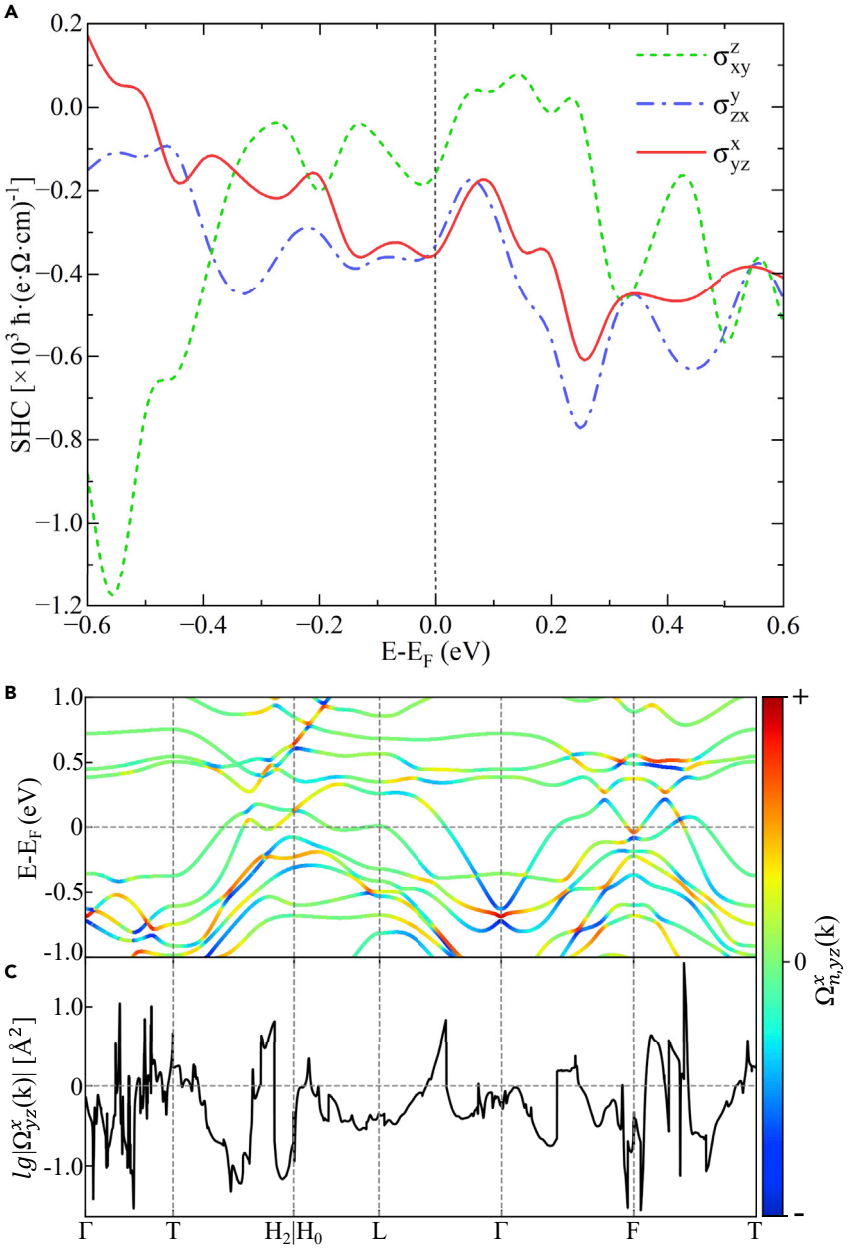

Figure 4. The intrinsic spin Hall effect of Ti_6Bi_4

(A) Three independent components of spin Hall conductivity (SHC) tensor as a function of chemical potential for Ti_6Bi_4.

(B) The band structure of Ti_6Bi_4 weighted by spin Berry curvature $\Omega^x_{n,yz}(\mathbf{k})$.

(C) The k-resolved $\Omega^x_{yz}(\mathbf{k})$ by integrating the spin Berry curvature of all occupied bands along the high-symmetry paths at E_F.

0.121 eV, which may be synthesized experimentally. Their structural information, E_f and E_{hull}, are summarized in Table S2.

Similar to the analysis of Ti_6Bi_4, we also calculate the topological properties, electronic structures, superconducting properties, and SHC of these Ti_6X_4 members. Ti_6Sb_4 has similar energy bands to that of Ti_6Bi_4. The DOS of Ti_6Sb_4 and Ti_6Pb_4 maintains the valley characteristic near E_F similar to that of Ti_6Bi_4, while the DOS of Ti_6Tl_4 and Ti_6In_4 shows different behaviors. As plotted in Figures S5–S8, abundant TSS are obtained in projected spectral functions for all members of Ti_6X_4, and the bands near Fermi level with a nonzero $\mathbb{Z}_2$

Table 2. Three independent components of SHC ($\hbar\cdot$ (e $\cdot\Omega\cdot$ cm)$^{-1}$) at the Fermi energy for Ti_6X_4

SHC ($\hbar\cdot$ (e $\cdot\Omega\cdot$ cm)$^{-1}$)	Ti_6Bi_4	Ti_6Sb_4	Ti_6Pb_4	Ti_6In_4	Ti_6Tl_4
σ^z_{xy}	−160	−225	−420	−274	−201
σ^y_{zx}	−333	−629	−230	−66	80
σ^x_{yz}	−354	−342	−124	34	−114

index indicate that they are topologically nontrivial, which show that these compounds are also $\mathbb{Z}_2$ topological metals. To study the superconductivity of the members of Ti_6X_4, we calculate α^2 F(ω), ω_{log}, EPC λ, and Tc at ambient pressure, as listed in Table 1. All other members of Ti_6X_4 have higher Tcs than Ti_6Bi_4, among which Ti_6Tl_4 has the highest Tc of 5.1 K. Ti_6Sb_4 has a larger ω_{log} due to the higher vibrational frequency of lighter Sb atom, leading to a larger Tc. Ti_6Pb_4, Ti_6In_4, and Ti_6Tl_4 have higher Tcs mainly because they are equivalent to hole doping of Ti_6Bi_4, resulting in higher DOS and EPC λ. The energy bands of other members of Ti_6X_4 in Figures S5–S8 also exhibit abundant gapped nodes and DNLs similar to Ti_6Bi_4, which contribute the SHC around 34–629 $\hbar\cdot$ (e $\cdot\Omega\cdot$ cm) $^{-1}$ at E_F as listed in Table 2. These values are comparable to some reported compounds with high SHC, such as V_6Sb_4 [204–537 $\hbar\cdot$ (e $\cdot\Omega\cdot$ cm)$^{-1}$],[64] $Bi_{1-x}Sb_x$ [474 $\hbar\cdot$ (e $\cdot\Omega\cdot$ cm)$^{-1}$],[65] and (Mo/W)Te_2 [18–361 $\hbar\cdot$ (e $\cdot\Omega\cdot$ cm)$^{-1}$].[66] The excellent stability, high SHC, and the combination of high Tc and nontrivial topology make kagome family Ti_6X_4 worth exploring experimentally.

DISCUSSIONS

We notice that a cousin material of AV_3Sb_5 — V_6Sb_4, which share the same protype structure with Ti_6X_4, has also been synthesized recently.[67,68] To explore the reason why in experiment V_6Sb_4 does not show signal of superconducting transition under pressure of 0 — 80 GPa,[67] we analyze the magnetic properties of V_6Sb_4 using the same calculation method for Ti_6X_4. We find that V_6Sb_4 is a ferromagnet with a small magnetic moment of 0.35 μ_B/f.u., which may explain the disappearance of superconductivity. Consistent with our calculations, the experimental magnetic susceptibility measurements showed that a small effective magnetic moment can indeed be measured despite the presence of impurities in V_6Sb_4.[68] In contrast, the nonmagnetic kagome family members Ti_6X_4 show high Tc, which deserves further experimental study.

To study the superconductivity in Ti_6Bi_4 as a function of pressure, we calculate its Tc at high pressures of 10 and 50 GPa and our results show that the pressure strongly suppresses its Tc (see Table S1). On the other hand, it is expected that the Tc of Ti_6Bi_4 can be enhanced by doping. It is noteworthy that the electronic DOS of Ti_6Bi_4 is located in a valley at the E_F in Figure 2A. By either electron or hole doping, the DOS can be greatly increased, and Tc may be improved correspondingly. So, the substitutional doping of Bi with elements of adjacent IIIA, IVA, and VIA groups is a promising carrier dopant, which slightly changes the kagome nets of Ti atoms and the band structure near the Fermi level. These predictions can be checked by further experiments.

The coexistence of the superconducting ground state and clear TSS near E_F in Ti_6Bi_4 is similar to the behaviors of CsV_3Sb_5. Since the possible Majorana bound state is discussed in the experiment of CsV_3Sb_5,[35] the Majorana bound state is also expected in Ti_6Bi_4 due to the proximity effect. On the other hand, we notice that the Fermi surface of Ti_6Bi_4 encloses five TRIM of F, F_1, F_2, Γ, and T as shown in Figures 2C and 2D, which shows a similar characteristic like odd-parity superconductors $Sn_{1-x}In_xTe$[13] and $Cu_xBi_2Se_3$.[10,11] A concise theorem shows that an odd-parity superconductor with inversion symmetry is a TSC if its Fermi surface encloses an odd number of TRIM in the BZ.[5,6,11] Although we only calculate superconductivity based on the traditional s-wave-paired BCS theory, Ti_6Bi_4 is likely to have an odd-parity pairing potential beyond traditional s-wave pairing due to its strong SOC like $Sn_{1-x}In_xTe$[13] and $Cu_xBi_2Se_3$.[11,12] Under this presumption of odd-parity superconductor, although Tc of Ti_6Bi_4 may be changed, the characteristic of the Fermi surface indicates that Ti_6Bi_4 is a strong TSC. Therefore, Ti_6Bi_4 can serve as a promising platform for investigating Majorana zero-modes and TSC.

Conclusions

To summarize, we predict a promising kagome family — Ti_6X_4 (X = Bi, Sb, Pd, Tl, and In) by DFT calculations. The thermodynamic and dynamic stability of these compounds is corroborated by the calculations of energy and phonon spectra. All members of Ti_6X_4 produce a superconducting transition with a Tc of 3.8

− 5.1 K and have a strong $\mathbb{Z}_2$ index with clear TSS near the Fermi level. The calculated spin texture of Ti_6Bi_4 shows TSS with spin helicity. Either the proximity-induced s-wave pairing on the surface or the possible odd-parity pairing with strong topological character shows that Ti_6Bi_4 is a promising TSC. Based on the Kubo formula, the SHC of Ti_6X_4 is calculated to be about $34 - 639\ \hbar\cdot(e\cdot\Omega\cdot cm)^{-1}$. The large SHC is attributed to the large spin Berry curvature caused by the gapped nodes and DNLs. With high EPC superconductivity, excellent topological properties, and large spin Hall effect, Ti_6X_4 deserve further experimental studies on their topological superconductivity and electronic transport properties.

Limitations of the study

We only calculate superconductivity based on the traditional s-wave-paired BCS theory. If Ti_6Bi_4 has an odd-parity pairing potential beyond traditional s-wave pairing due to its strong SOC, its superconducting temperature Tc may be changed.

STAR★METHODS

Detailed methods are provided in the online version of this paper and include the following:

- KEY RESOURCES TABLE
- RESOURCE AVAILABILITY
  - Lead contact
  - Materials availability
  - Data and code availability
- EXPERIMENTAL MODEL AND SUBJECT DETAILS
- METHOD DETAILS
  - DFT and superconductivity calculations
  - Calculations of topological properties and SHC
- QUANTIFICATION AND STATISTICAL ANALYSIS
- ADDITIONAL RESOURCES

SUPPLEMENTAL INFORMATION

Supplemental information can be found online at https://doi.org/10.1016/j.isci.2022.105813.

ACKNOWLEDGMENTS

This work is supported in part by the National Key R&D Program of China (Grant No. 2018YFA0305800), the Strategic Priority Research Program of the Chinese Academy of Sciences (Grants No. XDB28000000), the National Natural Science Foundation of China (Grant No.11834014), and High-magnetic field center of Chinese Academy of Sciences. B.G. is supported in part by the National Natural Science Foundation of China (Grant No. 12074378), the Chinese Academy of Sciences (Grants No. YSBR-030, No. Y929013EA2), the Strategic Priority Research Program of Chinese Academy of Sciences (Grant No. XDB33000000), and the Beijing Natural Science Foundation (Grant No. Z190011).

AUTHOR CONTRIBUTIONS

G.S. designed and supervised the research. X.W.Y. performed theoretical calculation. All of the authors participated in analyzing results. X.W.Y., J.Y.Y., B.G., and G.S. prepared the figures and the manuscript.

DECLARATION OF INTERESTS

The authors declare no competing interests.

Received: October 26, 2022
Revised: November 29, 2022
Accepted: December 12, 2022
Published: January 20, 2023

REFERENCES

1. Qi, X.-L., and Zhang, S.-C. (2011). Topological insulators and superconductors. Rev. Mod. Phys. *83*, 1057–1110. https://doi.org/10.1103/RevModPhys.83.1057.

2. Alicea, J. (2012). New directions in the pursuit of majorana fermions in solid state systems. Rep. Prog. Phys. *75*, 076501. https://doi.org/10.1088/0034-4885/75/7/076501.

3. Kitaev, A. (2003). Fault-tolerant quantum computation by anyons. Ann. Phys. *303*, 2–30. https://doi.org/10.1016/S0003-4916(02)00018-0.

4. Nayak, C., Simon, S.H., Stern, A., Freedman, M., and Das Sarma, S. (2008). Non-abelian anyons and topological quantum computation. Rev. Mod. Phys. *80*, 1083–1159. https://doi.org/10.1103/RevModPhys.80.1083.

5. Sato, M. (2009). Topological properties of spin-triplet superconductors and Fermi surface topology in the normal state. Phys. Rev. B *79*, 214526. https://doi.org/10.1103/PhysRevB.79.214526.

6. Sato, M. (2010). Topological odd-parity superconductors. Phys. Rev. B *81*, 220504. https://doi.org/10.1103/PhysRevB.81.220504.

7. Fu, L., and Kane, C.L. (2008). Superconducting proximity effect and Majorana Fermions at the surface of a topological insulator. Phys. Rev. Lett. *100*, 096407. https://doi.org/10.1103/PhysRevLett.100.096407.

8. Lutchyn, R.M., Sau, J.D., and Das Sarma, S. (2010). Majorana Fermions and a topological phase transition in semiconductor-superconductor heterostructures. Phys. Rev. Lett. *105*, 077001. https://doi.org/10.1103/PhysRevLett.105.077001.

9. Oreg, Y., Refael, G., and von Oppen, F. (2010). Helical liquids and Majorana bound states in quantum wires. Phys. Rev. Lett. *105*, 177002. https://doi.org/10.1103/PhysRevLett.105.177002.

10. Sasaki, S., Kriener, M., Segawa, K., Yada, K., Tanaka, Y., Sato, M., and Ando, Y. (2011). Topological superconductivity in $Cu_xBi_2Se_3$. Phys. Rev. Lett. *107*, 217001. https://doi.org/10.1103/PhysRevLett.107.217001.

11. Fu, L., and Berg, E. (2010). Odd-parity topological superconductors: theory and application to $Cu_xBi_2Se_3$. Phys. Rev. Lett. *105*, 097001. https://doi.org/10.1103/PhysRevLett.105.097001.

12. Hsieh, T.H., and Fu, L. (2012). Majorana Fermions and exotic surface andreev bound states in topological superconductors: application to $Cu_xBi_2Se_3$. Phys. Rev. Lett. *108*, 107005. https://doi.org/10.1103/PhysRevLett.108.107005.

13. Sasaki, S., Ren, Z., Taskin, A.A., Segawa, K., Fu, L., and Ando, Y. (2012). Odd-parity pairing and topological superconductivity in a strongly spin-orbit coupled semiconductor. Phys. Rev. Lett. *109*, 217004. https://doi.org/10.1103/PhysRevLett.109.217004.

14. Xu, J.-P., Liu, C., Wang, M.-X., Ge, J., Liu, Z.-L., Yang, X., Chen, Y., Liu, Y., Xu, Z.-A., Gao, C.-L., et al. (2014). Artificial topological superconductor by the proximity effect. Phys. Rev. Lett. *112*, 217001. https://doi.org/10.1103/PhysRevLett.112.217001.

15. Xu, J.P., Wang, M.X., Liu, Z.L., Ge, J.F., Yang, X., Liu, C., Xu, Z.A., Guan, D., Gao, C.L., Qian, D., et al. (2015). Experimental detection of a majorana mode in the core of a magnetic vortex inside a topological insulator-superconductor $Bi_2Te_3/NbSe_2$ heterostructure. Phys. Rev. Lett. *114*, 017001. https://doi.org/10.1103/PhysRevLett.114.017001.

16. Sun, H.H., Zhang, K.W., Hu, L.H., Li, C., Wang, G.Y., Ma, H.Y., Xu, Z.A., Gao, C.L., Guan, D.D., Li, Y.Y., et al. (2016). Majorana zero mode detected with spin selective andreev reflection in the vortex of a topological superconductor. Phys. Rev. Lett. *116*, 257003. https://doi.org/10.1103/PhysRevLett.116.257003.

17. Albrecht, S.M., Higginbotham, A.P., Madsen, M., Kuemmeth, F., Jespersen, T.S., Nygård, J., Krogstrup, P., and Marcus, C.M. (2016). Exponential protection of zero modes in Majorana islands. Nature *531*, 206–209. https://doi.org/10.1038/nature17162.

18. Mourik, V., Zuo, K., Frolov, S.M., Plissard, S.R., Bakkers, E.P.A.M., and Kouwenhoven, L.P. (2012). Signatures of Majorana Fermions in hybrid superconductor-semiconductor nanowire devices. Science *336*, 1003–1007. https://doi.org/10.1126/science.1222360.

19. Nadj-Perge, S., Drozdov, I.K., Li, J., Chen, H., Jeon, S., Seo, J., MacDonald, A.H., Bernevig, B.A., and Yazdani, A. (2014). Observation of Majorana Fermions in ferromagnetic atomic chains on a superconductor. Science *346*, 602–607. https://doi.org/10.1126/science.1259327.

20. You, J.-Y., Gu, B., Su, G., and Feng, Y.P. (2021). Two-dimensional topological superconductivity candidate in a van der Waals layered material. Phys. Rev. B *103*, 104503. https://doi.org/10.1103/PhysRevB.103.104503.

21. Dong, W.-H., Zhang, Y.-Y., Zhang, Y.-F., Sun, J.-T., Liu, F., and Du, S. (2022). Superconductivity and topological aspects of two-dimensional transition-metal monohalides. NPJ Comput. Mater. *8*, 185. https://doi.org/10.1038/s41524-022-00871-y.

22. You, J.Y., Gu, B., Su, G., and Feng, Y.P. (2022). Emergent kagome electrides. J. Am. Chem. Soc. *144*, 5527–5534. https://doi.org/10.1021/jacs.2c00177.

23. Zhang, J.-F., Guo, P.-J., Gao, M., Liu, K., and Lu, Z.-Y. (2019). β–$RhPb_2$: a topological superconductor candidate. Phys. Rev. B *99*, 045110. https://doi.org/10.1103/PhysRevB.99.045110.

24. Jin, K.-H., Huang, H., Mei, J.-W., Liu, Z., Lim, L.-K., and Liu, F. (2019). Topological superconducting phase in high-tc superconductor MgB_2 with Dirac–nodal-line fermions. NPJ Comput. Mater. *5*, 57. https://doi.org/10.1038/s41524-019-0191-2.

25. Huang, Z., Liu, W.L., Wang, H.Y., Su, Y.L., Liu, Z.T., Shi, X.B., Gao, S.Y., Chen, Z.Y., Yan, Y.J., Jiang, Z.C., et al. (2022). Dual topological states in the layered titanium-based oxypnictide superconductor $BaTi_2Sb_2O$. NPJ Quantum Mater. *7*, 70. https://doi.org/10.1038/s41535-022-00477-z.

26. Xu, G., Lian, B., Tang, P., Qi, X.L., and Zhang, S.C. (2016). Topological superconductivity on the surface of Fe-based superconductors. Phys. Rev. Lett. *117*, 047001. https://doi.org/10.1103/PhysRevLett.117.047001.

27. Zhu, S., Kong, L., Cao, L., Chen, H., Papaj, M., Du, S., Xing, Y., Liu, W., Wang, D., Shen, C., et al. (2020). Nearly quantized conductance plateau of vortex zero mode in an iron-based superconductor. Science *367*, 189–192. https://doi.org/10.1126/science.aax0274.

28. Wang, D., Kong, L., Fan, P., Chen, H., Zhu, S., Liu, W., Cao, L., Sun, Y., Du, S., Schneeloch, J., et al. (2018). Evidence for majorana bound states in an iron-based superconductor. Science *362*, 333–335. https://doi.org/10.1126/science.aao1797.

29. Zhang, P., Yaji, K., Hashimoto, T., Ota, Y., Kondo, T., Okazaki, K., Wang, Z., Wen, J., Gu, G.D., Ding, H., and Shin, S. (2018). Observation of topological superconductivity on the surface of an iron-based superconductor. Science *360*, 182–186. https://doi.org/10.1126/science.aan4596.

30. Chiu, C.K., Machida, T., Huang, Y., Hanaguri, T., and Zhang, F.C. (2020). Scalable Majorana vortex modes in iron-based superconductors. Sci. Adv. *6*, eaay0443. https://doi.org/10.1126/sciadv.aay0443.

31. Liu, W., Cao, L., Zhu, S., Kong, L., Wang, G., Papaj, M., Zhang, P., Liu, Y.B., Chen, H., Li, G., et al. (2020). A new Majorana platform in an Fe-As bilayer superconductor. Nat. Commun. *11*, 5688. https://doi.org/10.1038/s41467-020-19487-1.

32. Kong, L., Cao, L., Zhu, S., Papaj, M., Dai, G., Li, G., Fan, P., Liu, W., Yang, F., Wang, X., et al. (2021). Majorana zero modes in impurity-assisted vortex of lifeas superconductor. Nat. Commun. *12*, 4146. https://doi.org/10.1038/s41467-021-24372-6.

33. Li, M., Li, G., Cao, L., Zhou, X., Wang, X., Jin, C., Chiu, C.K., Pennycook, S.J., Wang, Z., and Gao, H.J. (2022). Ordered and tunable majorana-zero-mode lattice in naturally strained LiFeAs. Nature *606*, 890–895. https://doi.org/10.1038/s41586-022-04744-8.

34. Yuan, Y., Pan, J., Wang, X., Fang, Y., Song, C., Wang, L., He, K., Ma, X., Zhang, H., Huang, F., et al. (2019). Evidence of anisotropic majorana bound states in 2M-WS_2. Nat. Phys. *15*, 1046–1051. https://doi.org/10.1038/s41567-019-0576-7.

35. Liang, Z., Hou, X., Zhang, F., Ma, W., Wu, P., Zhang, Z., Yu, F., Ying, J.J., Jiang, K., Shan, L., et al. (2021). Three-dimensional charge density wave and surface-dependent vortex-core states in a kagome superconductor CsV_3Sb_5. Phys. Rev. X *11*, 031026. https://doi.org/10.1103/PhysRevX.11.031026.

36. Ortiz, B.R., Teicher, S.M.L., Hu, Y., Zuo, J.L., Sarte, P.M., Schueller, E.C., Abeykoon, A.M.M., Krogstad, M.J., Rosenkranz, S., Osborn, R., et al. (2020). CsV_3Sb_5: a Z_2 topological kagome metal with a superconducting ground state. Phys. Rev. Lett. *125*, 247002. https://doi.org/10.1103/PhysRevLett.125.247002.

37. Ortiz, B.R., Sarte, P.M., Kenney, E.M., Graf, M.J., Teicher, S.M.L., Seshadri, R., and Wilson, S.D. (2021). Superconductivity in the Z_2 kagome metal KV_3Sb_5. Phys. Rev. Materials *5*, 034801. https://doi.org/10.1103/PhysRevMaterials.5.034801.

38. Yin, Q., Tu, Z., Gong, C., Fu, Y., Yan, S., and Lei, H. (2021). Superconductivity and normal-state properties of kagome metal RbV_3Sb_5 single crystals. Chinese Phys. Lett. *38*, 037403. https://doi.org/10.1088/0256-307x/38/3/037403.

39. Song, Y., Ying, T., Chen, X., Han, X., Wu, X., Schnyder, A.P., Huang, Y., Guo, J.-g., and Chen, X. (2021). Competition of superconductivity and charge density wave in selective oxidized CsV_3Sb_5 thin flakes. Phys. Rev. Lett. *127*, 237001. https://doi.org/10.1103/PhysRevLett.127.237001.

40. Yang, H., Huang, Z., Zhang, Y., Zhao, Z., Shi, J., Luo, H., et al. (2022). Titanium doped kagome superconductor $CsV_{3-x}Ti_xSb_5$ and two distinct phases. Sci. Bull. *67*, 2176–2185. https://doi.org/10.1016/j.scib.2022.10.015.

41. Liu, Y., Wang, Y., Cai, Y., Hao, Z., Ma, X.-M., Wang, L., Liu, C., Chen, J., Zhou, L., Wang, J., et al. (2021). Doping evolution of superconductivity, charge order and band topology in hole-doped topological kagome superconductors $Cs(V_{1-x}Ti_x)_3Sb_5$. Preprint at arXiv. https://doi.org/10.48550/arXiv.2110.12651.

42. Chen, K.Y., Wang, N.N., Yin, Q.W., Gu, Y.H., Jiang, K., Tu, Z.J., Gong, C.S., Uwatoko, Y., Sun, J.P., Lei, H.C., et al. (2021). Double superconducting dome and triple enhancement of Tc in the kagome superconductor CsV_3Sb_5 under high pressure. Phys. Rev. Lett. *126*, 247001. https://doi.org/10.1103/PhysRevLett.126.247001.

43. Du, F., Luo, S., Ortiz, B.R., Chen, Y., Duan, W., Zhang, D., Lu, X., Wilson, S.D., Song, Y., and Yuan, H. (2021). Pressure-induced double superconducting domes and charge instability in the kagome metal KV_3Sb_5. Phys. Rev. B *103*, L220504. https://doi.org/10.1103/PhysRevB.103.L220504.

44. Li, H., Zhang, T., Yilmaz, T., Pai, Y., Marvinney, C., Said, A., Yin, Q., Gong, C., Tu, Z., Vescovo, E., et al. (2021). Observation of unconventional charge density wave without acoustic phonon anomaly in kagome superconductors AV_3Sb_5 (*A=Rb, Cs*). Phys. Rev. X *11*, 031050. https://doi.org/10.1103/PhysRevX.11.031050.

45. Nakayama, K., Li, Y., Kato, T., Liu, M., Wang, Z., Takahashi, T., Yao, Y., and Sato, T. (2022). Carrier injection and manipulation of charge-density wave in kagome superconductor CsV_3Sb_5. Phys. Rev. X *12*, 011001. https://doi.org/10.1103/PhysRevX.12.011001.

46. Yu, F.H., Ma, D.H., Zhuo, W.Z., Liu, S.Q., Wen, X.K., Lei, B., Ying, J.J., and Chen, X.H. (2021). Unusual competition of superconductivity and charge-density-wave state in a compressed topological kagome metal. Nat. Commun. *12*, 3645. https://doi.org/10.1038/s41467-021-23928-w.

47. Yu, F., Zhu, X., Wen, X., Gui, Z., Li, Z., Han, Y., Wu, T., Wang, Z., Xiang, Z., Qiao, Z., et al. (2022). Pressure-induced dimensional crossover in a kagome superconductor. Phys. Rev. Lett. *128*, 077001. https://doi.org/10.1103/PhysRevLett.128.077001.

48. Zhu, C.C., Yang, X.F., Xia, W., Yin, Q.W., Wang, L.S., Zhao, C.C., Dai, D.Z., Tu, C.P., Song, B.Q., Tao, Z.C., et al. (2022). Double-dome superconductivity under pressure in the v-based kagome metals AV_3Sb_5 (A=Rb and K). Phys. Rev. B *105*, 094507. https://doi.org/10.1103/PhysRevB.105.094507.

49. Hu, Y., Teicher, S.M., Ortiz, B.R., Luo, Y., Peng, S., Huai, L., Ma, J., Plumb, N.C., Wilson, S.D., He, J., and Shi, M. (2022). Topological surface states and flat bands in the kagome superconductor CsV_3Sb_5. Sci. Bull. *67*, 495–500. https://doi.org/10.1016/j.scib.2021.11.026.

50. Ortiz, B.R., Gomes, L.C., Morey, J.R., Winiarski, M., Bordelon, M., Mangum, J.S., Oswald, I.W.H., Rodriguez-Rivera, J.A., Neilson, J.R., Wilson, S.D., et al. (2019). New kagome prototype materials: discovery of KV_3Sb_5, RbV_3Sb_5, and CsV_3Sb_5. Phys. Rev. Materials *3*, 094407. https://doi.org/10.1103/PhysRevMaterials.3.094407.

51. Chen, H., Yang, H., Hu, B., Zhao, Z., Yuan, J., Xing, Y., Qian, G., Huang, Z., Li, G., Ye, Y., et al. (2021). Roton pair density wave in a strong-coupling kagome superconductor. Nature *599*, 222–228. https://doi.org/10.1038/s41586-021-03983-5.

52. Nie, L., Sun, K., Ma, W., Song, D., Zheng, L., Liang, Z., Wu, P., Yu, F., Li, J., Shan, M., et al. (2022). Charge-density-wave-driven electronic nematicity in a kagome superconductor. Nature *604*, 59–64. https://doi.org/10.1038/s41586-022-04493-8.

53. Yu, L., Wang, C., Zhang, Y., Sander, M., Ni, S., Lu, Z., Ma, S., Wang, Z., Zhao, Z., Chen, H., et al. (2021). Evidence of a hidden flux phase in the topological kagome metal CsV_3Sb_5. Preprint at arXiv. https://doi.org/10.48550/arXiv.2107.10714.

54. Feng, X., Jiang, K., Wang, Z., and Hu, J. (2021). Chiral flux phase in the kagome superconductor AV_3Sb_5. Sci. Bull. *66*, 1384–1388. https://doi.org/10.1016/j.scib.2021.04.043.

55. Jiang, Y.X., Yin, J.X., Denner, M.M., Shumiya, N., Ortiz, B.R., Xu, G., Guguchia, Z., He, J., Hossain, M.S., Liu, X., et al. (2021). Unconventional chiral charge order in kagome superconductor KV_3Sb_5. Nat. Mater. *20*, 1353–1357. https://doi.org/10.1038/s41563-021-01034-y.

56. Yang, H., Zhao, Z., Yi, X.-W., Liu, J., You, J.-Y., Zhang, Y., Guo, H., Lin, X., Shen, C., Chen, H., et al. (2022). Titanium-based kagome superconductor $CsTi_3Bi_5$ and topological states. Preprint at arXiv. https://doi.org/10.48550/arXiv.2209.03840.

57. Yi, X.-W., Ma, X.-Y., Zhang, Z., Liao, Z.-W., You, J.-Y., and Su, G. (2022). Large kagome family candidates with topological superconductivity and charge density waves. Phys. Rev. B *106*, L220505. https://doi.org/10.1103/PhysRevB.106.L220505.

58. Paier, J., Hirschl, R., Marsman, M., and Kresse, G. (2005). Commentary: the materials project: a materials genome approach to accelerating materials innovation. J. Chem. Phys. *122*, 234102. https://doi.org/10.1063/1.1926272.

59. Vassilev, G.P. (2006). Contribution to the Ti-Bi phase diagram. Cryst. Res. Technol. *41*, 349–357. https://doi.org/10.1002/crat.200510586.

60. Watanabe, K., and Yamane, H. (2016). Crystal structure of $TiBi_2$. Acta Crystallogr. E Crystallogr. Commun. *72*, 1254–1256. https://doi.org/10.1107/S2056989016012391.

61. Maruyama, S., Kado, Y., and Uda, T. (2013). Phase diagram investigations of the Bi-Ti system. J. Phase Equilib. Diffus. *34*, 289–296. https://doi.org/10.1007/s11669-013-0243-0.

62. Fu, L., and Kane, C.L. (2007). Topological insulators with inversion symmetry. Phys. Rev. B *76*, 045302. https://doi.org/10.1103/PhysRevB.76.045302.

63. Seemann, M., Ködderitzsch, D., Wimmer, S., and Ebert, H. (2015). Symmetry-imposed shape of linear response tensors. Phys. Rev. B *92*, 155138. https://doi.org/10.1103/PhysRevB.92.155138.

64. Yang, Y., Wang, R., Shi, M.Z., Wang, Z., Xiang, Z., and Chen, X.H. (2022). Symmetry-protected Dirac nodal lines and large spin Hall effect in a V_6Sb_4 kagome bilayer. Phys. Rev. B *105*, 155102. https://doi.org/10.1103/PhysRevB.105.155102.

65. Şahin, C., and Flatté, M.E. (2015). Tunable giant spin Hall conductivities in a strong spin-orbit semimetal: $Bi_{1-x}Sb_x$. Phys. Rev. Lett. *114*, 107201. https://doi.org/10.1103/PhysRevLett.114.107201.

66. Zhou, J., Qiao, J., Bournel, A., and Zhao, W. (2019). Intrinsic spin Hall conductivity of the semimetals $MoTe_2$ and WTe_2. Phys. Rev. B *99*, 060408. https://doi.org/10.1103/PhysRevB.99.060408.

67. Shi, M., Yu, F., Yang, Y., Meng, F., Lei, B., Luo, Y., Sun, Z., He, J., Wang, R., Jiang, Z., et al. (2022). A new class of bilayer kagome lattice compounds with Dirac nodal lines and pressure-induced superconductivity. Nat. Commun. *13*, 2773. https://doi.org/10.1038/s41467-022-30442-0.

68. Wang, N., Gu, Y., McGuire, M.A., Yan, J., Shi, L., Cui, Q., Chen, K., Wang, Y., Zhang, H., Yang, H., et al. (2022). A density-wave-like transition in the polycrystalline V_3Sb_2 sample with bilayer kagome lattice. Chinese Phys. B *31*, 017106. https://doi.org/10.1088/1674-1056/ac4227.

69. Kresse, G., and Furthmüller, J. (1996). Efficient iterative schemes for ab initio total-energy calculations using a plane-wave basis set. Phys. Rev. B Condens. Matter *54*, 11169–11186. https://doi.org/10.1103/physrevb.54.11169.

70. Giannozzi, P., Baroni, S., Bonini, N., Calandra, M., Car, R., Cavazzoni, C., Ceresoli, D., Chiarotti, G.L., Cococcioni, M., Dabo, I., et al. (2009). Quantum espresso: a modular and open-source software project for quantum simulations of materials. J. Phys. Condens. Matter *21*, 395502. https://doi.org/10.1088/0953-8984/21/39/395502.

71. Gao, J., Wu, Q., Persson, C., and Wang, Z. (2021). Irvsp: to obtain irreducible representations of electronic states in the vasp. Comput. Phys. Commun. *261*, 107760. https://doi.org/10.1016/j.cpc.2020.107760.

72. Mostofi, A.A., Yates, J.R., Pizzi, G., Lee, Y.-S., Souza, I., Vanderbilt, D., and Marzari, N. (2014). An updated version of wannier90: a tool for obtaining maximally-localised wannier functions. Comput. Phys. Commun. *185*, 2309–2310. https://doi.org/10.1016/j.cpc.2014.05.003.

73. Wu, Q., Zhang, S., Song, H.-F., Troyer, M., and Soluyanov, A.A. (2018). Wanniertools: an open-source software package for novel topological materials. Comput. Phys. Commun. *224*, 405–416. https://doi.org/10.1016/j.cpc.2017.09.033.

74. Blöchl, P. (1994). Projector augmented-wave method. Phys. Rev. B Condens. Matter *50*, 17953–17979. https://doi.org/10.1103/physrevb.50.17953.

75. Si, J.G., Lu, W.J., Sun, Y.P., Liu, P.F., and Wang, B.T. (2022). Charge density wave and pressure-dependent superconductivity in the kagome metal CsV_3Sb_5: a first-principles study. Phys. Rev. B *105*, 024517. https://doi.org/10.1103/PhysRevB.105.024517.

76. Baroni, S., de Gironcoli, S., Dal Corso, A., and Giannozzi, P. (2001). Phonons and related crystal properties from density-functional perturbation theory. Rev. Mod. Phys. *73*, 515–562. https://doi.org/10.1103/RevModPhys.73.515.

77. Allen, P.B., and Dynes, R.C. (1975). Transition temperature of strong-coupled superconductors reanalyzed. Phys. Rev. B *12*, 905–922. https://doi.org/10.1103/PhysRevB.12.905.

78. McMillan, W.L. (1968). Transition temperature of strong-coupled superconductors. Phys. Rev. *167*, 331–344. https://doi.org/10.1103/PhysRev.167.331.

79. Zhang, J.-F., Liu, K., and Lu, Z.-Y. (2021). First-principles study of the double-dome superconductivity in the kagome material CsV_3Sb_5 under pressure. Phys. Rev. B *104*, 195130. https://doi.org/10.1103/PhysRevB.104.195130.

80. Guo, G.Y., Yao, Y., and Niu, Q. (2005). Ab initio calculation of the intrinsic spin Hall effect in semiconductors. Phys. Rev. Lett. *94*, 226601. https://doi.org/10.1103/PhysRevLett.94.226601.

81. Sinova, J., Culcer, D., Niu, Q., Sinitsyn, N.A., Jungwirth, T., and MacDonald, A.H. (2004). Universal intrinsic spin Hall effect. Phys. Rev. Lett. *92*, 126603. https://doi.org/10.1103/PhysRevLett.92.126603.

82. Sancho, M.P.L., Sancho, J.M.L., Sancho, J.M.L., and Rubio, J. (1985). Highly convergent schemes for the calculation of bulk and surface green functions. J. Phys. F: Met. Phys. *15*, 851–858. https://doi.org/10.1088/0305-4608/15/4/009.

83. Zhang, H., Liu, C.X., and Zhang, S.C. (2013). Spin-orbital texture in topological insulators. Phys. Rev. Lett. *111*, 066801. https://doi.org/10.1103/PhysRevLett.111.066801.

84. Dai, X., Hughes, T.L., Qi, X.-L., Fang, Z., and Zhang, S.-C. (2008). Helical edge and surface states in hgte quantum wells and bulk insulators. Phys. Rev. B *77*, 125319. https://doi.org/10.1103/PhysRevB.77.125319.

STAR★METHODS

KEY RESOURCES TABLE

REAGENT or RESOURCE	SOURCE	IDENTIFIER
Software and algorithms		
Vienna ab initio simulation package	Kresse and Furthmüller[69]	www.vasp.at/
QUANTUM-ESPRESSO	Giannozzi et al.,[70]	www.quantum-espresso.org/
irvsp	Gao et al.,[71]	github.com/zjwang11/irvsp
Wannier90	Mostofi et al.,[72]	www.wannier.org/
WannierTools	Wu et al.,[73]	www.wanniertools.com/

RESOURCE AVAILABILITY

Lead contact

Further information and requests for resources and reagents should be directed to and will be fulfilled by the Lead Contact, Gang Su (gsu@ucas.ac.cn).

Materials availability

Detail of structures information can be seen in Table S2 of supplemental information.

Data and code availability

Data reported in this paper will be shared by the lead contact upon request. There is no code associated with this work. Any additional information required to reanalyze the data reported in this paper is available from the lead contact upon request.

EXPERIMENTAL MODEL AND SUBJECT DETAILS

This study does not use experimental methods typical in the life sciences.

METHOD DETAILS

DFT and superconductivity calculations

DFT calculations with projector augmented-wave pseudopotential method[74] are implemented through *Viennaab initio simulationpackage* (VASP)[69] and *QUANTUM − ESPRESSO* (QE).[70] The convergence criterion of atomic force is less than 1 meV/Å for VASP and 10^{-7} Ry/a.u. for QE (1a.u. = 0.053 nm). The cutoff energy of plane-wave is taken as 500 eV and the total energy convergence threshold of all processes is 10^{-7} eV/atom for VASP. For QE, kinetic energy cutoffs of wavefunction and charge density are taken as 100 Ry and 1250 Ry, respectively, and the convergence threshold cutoffs of wavefunction and ionic minimization total energy is 10^{-9} Ry. To be consistent with the previous calculations and experimental results of AV_3Sb_5,[50,75] the on-site Coulomb interaction (U) is set to 0 eV. The Γ centered 6 × 6 × 6 Monkhorst-Pack k-mesh is used in the self-consistent calculation. The q-point grid is set to 3 × 3 × 3 during EPC calculation. The symmetry analysis of the structure and parity calculation of the time-reversal invariant momenta (TRIM) points are performed by the *irvsp* program.[71]

The phonon dispersion and EPC are calculated by the phonon module of QE using the density functional perturbation theory.[76] To estimate Tc, we use the McMillan-Allen-Dynes equation,[77,78]

$$T_c = \frac{\omega_{log}}{1.2}\exp\left[-\frac{1.04(1+\lambda)}{\lambda - \mu^*(1+0.62\lambda)}\right], \quad \text{(Equation 1)}$$

where ω_{log} is the logarithmically averaged phonon frequency, and λ is a dimensionless parameter describing the EPC strength. The semiempirical Coulomb pseudopotential μ^* of electron-electron effective repulsion is taken as 0.10, which is consistent with the previous calculation of AV_3Sb_5.[75,79]

After careful testing, we find that the Tc with and without SOC are almost the same. Therefore, the calculation of superconductivity in this article does not include SOC.

Calculations of topological properties and SHC

We use the *Wannier*90 package[72] to fit the Wannier functions, construct effective tight-binding Hamiltonian, and calculate spin Hall conductivity (SHC), where Ti-d and Bi-p orbitals are chosen to be projected.

SHC tensor is calculated by employing the Kubo formula[80,81]

$$\sigma_{\alpha\beta}^{\gamma} = e\hbar \int \frac{d\mathbf{k}}{(2\pi)^3} \Omega_{\alpha\beta}^{\gamma}(\mathbf{k}), \quad \text{(Equation 2)}$$

$$\Omega_{\alpha\beta}^{\gamma}(\mathbf{k}) = \sum_{n} f_{n\mathbf{k}} \Omega_{n,\alpha\beta}^{\gamma}(\mathbf{k}), \quad \text{(Equation 3)}$$

$$\Omega_{n,\alpha\beta}^{\gamma}(\mathbf{k}) = -2\mathrm{Im} \sum_{m \neq n} \frac{\langle \psi_{n\mathbf{k}} | j_{\alpha}^{\gamma} | \psi_{m\mathbf{k}} \rangle \langle \psi_{m\mathbf{k}} | v_{\beta} | \psi_{n\mathbf{k}} \rangle}{(E_{m\mathbf{k}} - E_{n\mathbf{k}})^2}, \quad \text{(Equation 4)}$$

where $\Omega_{n,\alpha\beta}^{\gamma}(\mathbf{k})$ is the spin Berry curvature, $\Omega_{\alpha\beta}^{\gamma}(\mathbf{k})$ is the k-resolved term obtained by integrating the spin Berry curvature of all occupied bands, which is the derivative of the SHC to $\mathbf{k}$, and $f_{n\mathbf{k}}$ is the Fermi-Dirac distribution. The spin current operator $j_{\alpha}^{\gamma} = 1/2\{v_{\alpha}, s^{\gamma}\}$ with velocity operator $v_{\alpha} = \frac{1}{\hbar}\frac{\partial H}{\partial k_{\alpha}}(\alpha, \beta, \gamma = x, y, z)$ and spin operator s^{γ}. The spin current operator can be expressed as $j_{\alpha}^{\gamma} = \sigma_{\alpha\beta}^{\gamma} E_{\beta}$. The k-mesh for the spin Berry curvature integral adopts 200 × 200 × 200, and an extra 5 × 5 × 5 fine mesh around those points with $\Omega_{n,\alpha\beta}^{\gamma}(\mathbf{k})$ exceeding 100 $\mathring{A}^2$ is added. SOC is considered in SHC calculation.

With effective tight-binding Hamiltonian, we calculate the surface spectra and topological properties using the iterative surface Green's function method with *WannierTools* package.[73,82] After calculating the surface Green's function for a semi-infinite system $G_s(\mathbf{k}_{\parallel}, \omega + i\eta)$. The surface spectrum function $A(\mathbf{k}_{\parallel}, \omega)$ can be obtained from its imaginary part, with which we can identify clear topological surface states of specific materials. The spin texture of surface states can be obtained with

$$\mathbf{S}(\mathbf{k}_{\parallel}, \omega) = -\frac{1}{\pi} \lim_{\eta \to 0^+} \mathrm{ImTr}[\sigma G_s(\mathbf{k}_{\parallel}, \omega + i\eta)] \,/\, A(\mathbf{k}_{\parallel}, \omega) \quad \text{(Equation 5)}$$

where σ are the Pauli matrices and $\mathbf{k}_{\parallel}$ is the 2D momentum.[83,84]

QUANTIFICATION AND STATISTICAL ANALYSIS

Our study does not include statistical analysis or quantification.

ADDITIONAL RESOURCES

There are no additional resources needed to be declared in this manuscript, additional requests for this can be made by contacting the lead contact.